Impact of QSW-ZVS on Input EMI Filter Design in DC-DC Converters

International Journal of Circuit Theory and Applications

WILEY

ORIGINAL ARTICLE OPEN ACCESS

Impact of QSW-ZVS on Input EMI Filter Design in DC-DC Converters

Silvia Simone[1] | Amirali Hosseini[2] | Francesco Gabriele[1] | Fabio Pareschi[1]

[1]Department of Electronics and Telecommunications, Politecnico di Torino, Turin, Italy | [2]Department of Electrical, Computer and Biomedical Engineering, Università di Pavia, Pavia, Italy

Correspondence: Silvia Simone (silvia_simone@polito.it)

Received: 5 February 2026 | **Revised:** 31 March 2026 | **Accepted:** 3 April 2026

Keywords: damping network | DC-DC buck converter | extra element theorem | passive EMI filter | quasi-square-wave zero-voltage switching | small-signal model

ABSTRACT

This paper investigates the impact of the quasi-square wave zero voltage switching (QSW-ZVS) technique on the design of passive electromagnetic interference (EMI) filters for DC-DC buck converters. A standard design-oriented analysis is conducted, focusing on a single-stage LC EMI filter with a single-resistor shunt damping network R_d-C_d, aiming to minimize the impact of the filter on the small-signal dynamic of the converter. We demonstrate that QSW-ZVS enables a reduction in the size of the damping network of the EMI filter when compared with conventional hard-switching designs. Furthermore, we generalize the proposed analysis to different EMI filter cutoff frequencies, evaluating how the value of the shunt damping capacitance C_d varies when QSW-ZVS is enabled. Both the proposed small-signal model and the design methodology are validated with SIMPLIS simulations under various operating conditions of a DC-DC buck converter.

1 | Introduction

DC-DC converters are ubiquitous power-conversion devices. They are extensively employed across a broad range of heterogeneous application areas, including automotive systems, renewable energy systems and consumer electronics [1, 2]. In these domains, minimizing power losses is of considerable importance, as it directly impacts energy efficiency, thermal management requirements and system reliability. Conventional hard-switching DC-DC converters are commonly employed owing to their architectural simplicity, straightforward design and cost-effectiveness. However, their operating mode is associated with high power losses, thus resulting in a low power conversion efficiency.

To mitigate this limitation, soft-switching techniques have been widely developed and are now well established in DC–DC converter applications as an effective means of reducing switching power losses and therefore improving the overall power conversion efficiency, as well as optimizing switching patterns [3]. Soft-switching techniques are commonly implemented in DC-DC converters to reduce switching power losses and so increase the overall power conversion efficiency. Among these, quasi-square wave zero voltage switching (QSW-ZVS) permits to achieve zero voltage switching (ZVS) without introducing additional circuit elements in the power stage of the converter [4, 5]. This is made possible by leveraging the intrinsic parasitic capacitance of the power semiconductor switches and the main filter inductor of conventional hard-switching power conversion topologies [6–8]. As an ancillary benefit, soft-switching also permits to mitigate the emission level of electromagnetic interference (EMI) produced by switching DC-DC converters [9, 10]. Indeed, it reduces the high dv/dt and di/dt that characterize the switching operation of traditional hard-switched DC-DC

converters. Consequently, smaller filtering components can be used in passive EMI filters to achieve the same EMI attenuation level and comply with EMI standards [11].

However, a substantial part of the overall EMI filter area is attributable to its damping circuit network. The latter is crucial in ensuring system stability, as it reduces the peak of the output impedance of the EMI filter, thus avoiding interaction with the input impedance of the converter. In practice, the design criteria of the damping network are derived from conventional averaged small-signal models of hard-switching DC-DC converters [12, 13]. Nevertheless, introducing a ZVS mechanism has a non-negligible impact on the converter dynamics [14, 15]. Referring to the QSW-ZVS Buck converter topology shown in Figure 1, an enhanced averaged small-signal model has been proposed in [16]. This model explicitly embeds the effect of the considered ZVS network. However, to the best of the authors' knowledge, the impact of a ZVS network on the design of EMI filters has not been investigated yet.

In this work, relying on the small-signal model developed in [16] we develop a framework for passive EMI filter design. In particular, we (i) extend the small-signal model proposed in [16], including a passive EMI filter; (ii) analyze the influence of a passive EMI filter on the main transfer functions (TFs) of the converter when QSW-ZVS is enabled, and (iii) propose an optimized design methodology for the damping network of passive EMI filters. As it will be demonstrated, traditional design approaches for the damping network of passive EMI filters are found to be conservative, resulting in an overestimation of the required component size of the damping elements. Conversely, the use of the derived QSW-ZVS-based design equations enables a more accurate sizing of the damping components, leading to a reduction in the overall physical area and volume of the EMI filter.

The rest of the paper is organized as follows. In Section 2, we develop a complete small-signal model for the converter shown in Figure 1, capturing the converter dynamics when a passive EMI filter is employed. In Section 3, the impact of the passive EMI filter on the converter dynamics is assessed. Furthermore, a practical design methodology is presented to ensure that the EMI filter does not alters the converter dynamics. In Section 4, the proposed model and design method are validated through SIMPLIS simulations, comparing QSW-ZVS and hard-switched designs. Finally, in Section 5, we draw the conclusion.

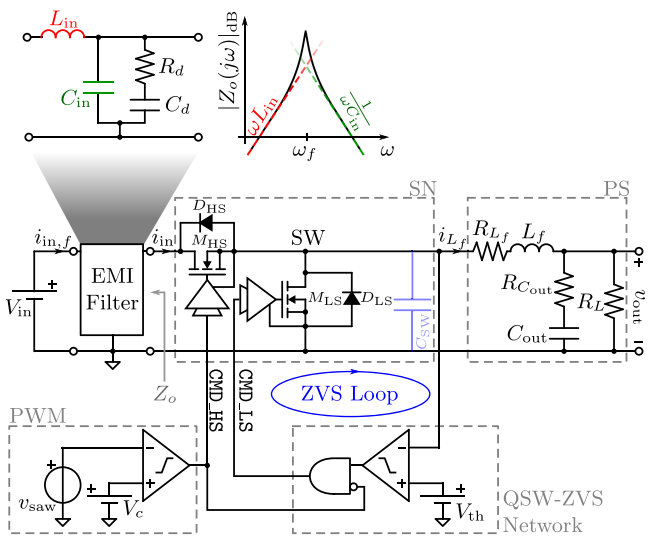

FIGURE 1 | Architecture of the QSW-ZVS DC-DC buck converter with EMI filter considered in this paper.

2 | The Averaged Small-Signal Model of QSW-ZVS Buck Converter and Passive EMI Filter

Averaged small-signal models are of paramount importance in the analysis and design of switching DC-DC converters. They permit to assess the dynamic behavior of the converters by modeling them as linear time-invariant systems. In the design of passive EMI filters, averaged small-signal models allow to evaluate the interaction between the converter and the EMI filter when they are interconnected. In practice, this requires to compute key TFs from the complete small-signal model of the converter [13, 17, 18].

In the following, we denote constant signals in capital letters, for example, U, and small-signal perturbations as $\tilde{u}$.

2.1 | The QSW-ZVS DC-DC Buck Converter Architecture

The QSW-ZVS DC-DC buck converter we consider is shown in Figure 1. The complete scheme includes the power stage (PS), the switching network (SN), the pulse-width modulator (PWM) stage, the QSW-ZVS network, and the passive EMI filter. The SN is implemented as a synchronous half-bridge comprising the Low-Side LS and High-Side (HS) power MOSFETs, that is, M_{LS} and M_{HS}, together with their body diodes, that is, D_{LS} and D_{HS}. The ON-state resistances of the LS and HS power MOSFETs are $R_{LS_{on}}$ and $R_{HS_{on}}$, respectively. The overall parasitic capacitance on the SW node is modeled with a linear capacitor C_{SW}. The SN is connected to the PS of the converter. The latter includes the inductor L_f and the output capacitor C_{out}, along with their equivalent series resistances (ESRs), that is, R_{L_f} and $R_{C_{out}}$, respectively. A fixed resistor R_L is connected to the output port of the converter to set the static load current level $I_{out} = V_{out}/R_L$, where V_{out} is the DC output voltage value. The power MOSFETs M_{LS} and M_{HS} are driven by the sawtooth-based PWM stage and the QSW-ZVS network that synthesize the logic driving signals CMD_HS and CMD_LS. The PWM stage compares the sawtooth-voltage V_{saw} and the control voltage V_c, generating CMD_HS. The frequency of the signal V_{saw} is equal to $F_{sw} = 1/T_{sw}$, while its amplitude is V_{pk}. The QSW-ZVS network senses the voltage on the SW node and compares it with the reference voltage V_{ref} to detect the optimal turn-ON time instant for M_{LS}, thereby implementing a break-before-make mechanism to generate CMD_LS.

The single-stage passive EMI filter is interposed between the input voltage source V_{in} and the SN. It smooths-out the current disturbance i_{in} generated by the converter through the filtering elements L_{in} and C_{in}. The single-resistor shunt damping network R_d-C_d reduces the resonant peak of the filter output impedance Z_o so that the interaction between the EMI filter and the converter is minimized. Further details on this aspect will be provided in the next sections.

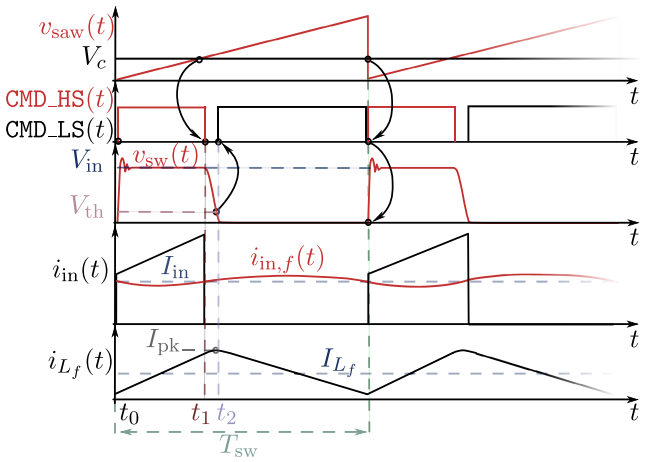

FIGURE 2 | Main voltage and current waveforms in QSW-ZVS operation of the converter in Figure 1.

The operation of the converter in steady-state is shown in Figure 2. At the beginning, that is, when $t = t_0$, $V_c > V_{saw}$, CMD_HS is asserted, and CMD_LS is deasserted. In turn, V_{SW} equals to V_{in} and the current flowing through L_f, namely, i_{L_f}, increases. When $t = t_1$, $V_c < V_{saw}$ and the signal CMD_HS becomes deasserted. The quasi-constant current $i_{L_f} \approx I_{pk}$ discharges the parasitic capacitance C_{SW}, whose terminal voltage in $t = t_1$ coincides with V_{SW}. An estimate of the current I_{pk} is given by the small-ripple approximation and inductor volt-second balance [18] as

$$I_{pk} = I_{L_f} + \frac{V_{in} - V_{out}}{2L_f} T_{on,0} = I_{L_f} + \frac{V_{in} - V_{out}}{2L_f F_{sw}} D_0, \tag{1}$$

where $T_{on,0} = t_1 - t_0$ is the ON time of the driving signal CMD_HS and $D_0 = T_{on,0}/T_{sw}$ is the correspondent duty-cycle. For $t > t_0$, the voltage V_{SW} starts decreasing, reaching the level $V_{SW} \approx V_{th} \ll V_{in}$ when $t = t_2$. Here, CMD_LS is asserted, thus turning-ON M_{LS} with low drain-source voltage and hence implementing ZVS for the LS MOSFET. Therefore, it should be noted that the action of the QSW-ZVS network is to introduce an adaptive dead-time interval $T_d := t_2 - t_1$ after the HS MOSFET is turned-OFF. The length of T_d is adaptively set based on the converter operating conditions, and an estimate of this interval is obtained by assuming a linear discharge of C_{SW} as $T_d = C_{SW} V_{in}/I_{pk}$. The EMI filter prevents that the pulsating input current i_{in} propagates back to the DC input voltage source. Indeed, the filtered current signal $i_{in,f}$ features a low-amplitude ripple signal superimposed on the DC input current component $I_{in} = D_0 I_{L_f}$.

2.2 | The Averaged Small-Signal Model

The equivalent averaged small-signal model for converter herein considered is proposed in Figure 3. From an high-level perspective, it embeds the equivalent small-signal model presented in [16], the PWM stage and the EMI filter stage. The correspondence between the small-signal model and the large-signal circuit is evident. The signal $\tilde{v}_{in}$ represents the line-voltage perturbation that propagates through the EMI filter. The control voltage perturbation $\tilde{v}_c$ translates into a duty-ratio perturbation $\tilde{d}_0$ through the TF of the PWM stage, that is, $1/V_{pk}$ [1]. The output current perturbation $\tilde{\imath}_{out}$ is applied to the output port of the converter, and it models the load-current variations. The

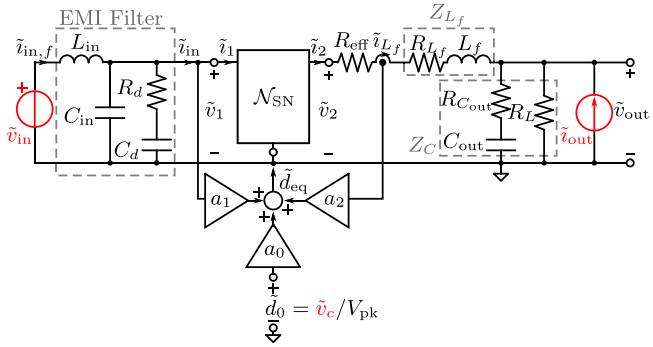

FIGURE 3 | The averaged small-signal model of the considered QSW-ZVS DC-DC Buck converter and the passive EMI filter.

TABLE 1 | Parameters and coefficients of the small-signal circuit model in Figure 3.

Parameter	Expression
e_0	$V_{in} - (R_{HS_{on}} I_{L_f} + R_{LS_{on}} I_{L_f})$
D_{eq}	$D_0 + T_d/(2T_{sw})$
R_{eff}	$R_{HS_{on}} D_{eq} + R_{LS_{on}}(1 - D_{eq})$
a_0	$1 - C_{SW} V_{in}(V_{in} - V_{out})/(4L_f I_{pk}^2)$
a_1	$C_{SW}/(2T_{sw} I_{pk})$
a_2	$-C_{SW} V_{in}/(2T_{sw} I_{pk}^2)$

two-port network $\mathcal{N}_{SN}$ models the behavior of the SN. The relationship between its input and output is derived by applying the standard circuit averaging technique [1] based on the terminal waveforms of the SN shown in Figure 2. At this stage, by neglecting the R_{eff}-induced ohmic losses, this yields

$$\mathcal{N}_{SN}: \begin{bmatrix} \tilde{V}_2 \\ \tilde{\imath}_1 \end{bmatrix} = \begin{bmatrix} D_{eq} & 0 \\ 0 & D_0 \end{bmatrix} \begin{bmatrix} \tilde{v}_1 \\ \tilde{\imath}_2 \end{bmatrix} + \underbrace{\begin{bmatrix} V_{in} & 0 \\ 0 & I_{L_f} \end{bmatrix} \begin{bmatrix} \tilde{d}_{eq} \\ \tilde{d}_0 \end{bmatrix}}_{\text{Ext. Control}}. \tag{2}$$

Then, an equivalent AC-resistance R_{eff} is introduced at the output port of the $\mathcal{N}_{SN}$ based on [19, 20], as shown in Figure 3. The gain stages a_0, a_1 and a_2 model the effect of the QSW-ZVS network. Their analytical expressions are summarized in Table 1, while for additional details on the mathematical derivation process the reader is referred to [16, 18]. Thus, the QSW-ZVS network modulates the external duty-cycle perturbation $\tilde{d}_0$ as

$$\tilde{d}_{eq} = a_0 \tilde{d}_0 + a_1 \tilde{V}_1 + a_2 \tilde{\imath}_{L_f}, \tag{3}$$

where $\tilde{v}_1$ is the small-signal voltage perturbation applied at the input port of the converter and $\tilde{\imath}_{L_f}$ is the small-signal variation of the inductor current. Also, it is worth noting that the averaged small-signal model in Figure 3 can be used to cover the scenario in which the QSW-ZVS network is disabled by simply imposing $a_0 = 1$, $a_1 = a_2 = 0$ and replacing D_{eq} with D_0. Here, in fact, $T_d = 0$ and CMD_LS is asserted as soon as CMD_HS is deasserted. In consequence, $\tilde{d}_{eq} = \tilde{d}_0$.

To better empathize the impact of the EMI filter on the small-signal dynamics of the converter, a high-level view of the small-signal model shown in Figure 3 is proposed in Figure 4. In the figure, the EMI filter and the small-signal input perturbation $\tilde{v}_{\text{in}}$ shown in Figure 3 are replaced by their Thévenin equivalent. The equivalent voltage source is $H_f \cdot \tilde{v}_{\text{in}}$, where

$$H_f(s) = \frac{\frac{1}{sC_{\text{in}}} \| (R_d + \frac{1}{sC_d})}{sL_{\text{in}} + \left(\frac{1}{sC_{\text{in}}} \| \left(R_d + \frac{1}{sC_d}\right)\right)}, \tag{4}$$

while the equivalent output impedance is computed as

$$Z_o(s) = sL_f \| \frac{1}{sC_{\text{in}}} \| \left(\frac{1}{sC_d} + R_d\right), \tag{5}$$

where s is the complex Laplace variable and $\|$ is the parallel operator.

Furthermore, the $\mathcal{N}_{\text{SN}}$ block models the SN. The high-level representation in Figure 4 provides a framework to derive any TF of the converter both when the input EMI filter is introduced/removed and by enabling/disabling the action of the QSW-ZVS network. In the following, the formulas associated with the traditional and QSW-ZVS cases are denoted by the superscripts $^{\text{Trad}}$ and $^{\text{ZVS}}$, respectively, whereas the superscript $^{\nu}$ denotes the general form of the expression, from which the $^{\text{Trad}}$ and $^{\text{ZVS}}$ cases are obtained.

In practice, the control-to-output TF $G_{\text{vc}}^{\nu}(s)$, the line-to-output TF $G_{\text{vg}}^{\nu}(s)$, and the output impedance TF $Z_{\text{out}}^{\nu}(s)$ are of major interest for design-oriented purposes. To maintain a clear exposition, we start by deriving these TFs assuming that the EMI filter is not present. This scenario is illustrated in Figure 4, where $Z_o = 0$ and $H_f = 1$ (and thus, $\tilde{v}_1 = \tilde{v}_{\text{in}}$). Also, here, we set $\tilde{v}_{\text{test}} = 0$, where $\tilde{v}_{\text{test}}$ is an external voltage excitation whose purpose will be clarified shortly. At this stage, the $\mathcal{N}_{\text{SN}}$ block is represented by the equivalent circuit model in Figure 3. Through simple algebraic manipulations, the control-to-output TF is derived as

$$G_{\text{vc}}^{\nu}(s)|_{Z_o(s)=0} = \frac{\tilde{V}_{\text{out}}(s)}{\tilde{V}_c(s)} = k_{\text{vc}}^{\nu} \frac{Z_2^{\nu}(s)}{Z_1^{\nu}(s) + Z_2^{\nu}(s)}, \tag{6}$$

where k_{vc}^{ν}, $Z_1^{\nu}(s)$, and $Z_2^{\nu}(s)$ are defined in Table 2. Similarly, the line-to-output TF is derived as

$$G_{\text{vg}}^{\nu}(s)|_{Z_o(s)=0} = \frac{\tilde{V}_{\text{out}}(s)}{\tilde{V}_{\text{in}}(s)} = k_{\text{vg}}^{\nu} \frac{Z_2^{\nu}(s)}{Z_1^{\nu}(s) + Z_2^{\nu}(s)}. \tag{7}$$

where k_{vg}^{ν} is defined in Table 2. Finally, the output impedance TF is given by

$$Z_{\text{out}}^{\nu}(s)|_{Z_o(s)=0} = \frac{\tilde{V}_{\text{out}}(s)}{\tilde{i}_{\text{out}}(s)} = Z_1^{\nu}(s) \| Z_2^{\nu}(s). \tag{8}$$

In order to contemplate the scenario in which the EMI filter is introduced, we resort to the Extra Element Theorem (EET) [1, 19, 21]. This theorem is applied to straightforwardly assess the impact of the EMI filter on the main converter TFs without requiring a full re-derivation from scratch. Therefore, it permits to preserve the main results in (6), (7), and (8), while the impact of the EMI filter is embedded in an additional correction factor. The new control-to-output TF of the converter is thus given by

$$G_{\text{vc}}^{\nu}(s) = G_{\text{vc}}^{\nu}(s)|_{Z_o=0} \cdot \frac{1 + Z_o(s)/Z_n^{\nu}(s)}{1 + Z_o(s)/Z_d^{\nu}(s)}, \tag{9}$$

the line-to-output transfer function becomes

$$G_{\text{vg}}^{\nu}(s) = H_f(s) \cdot G_{\text{vg}}^{\nu}(s)|_{Z_o=0} \cdot \frac{1 + Z_o(s)/Z_g^{\nu}(s)}{1 + Z_o(s)/Z_d^{\nu}(s)} \tag{10}$$

and the new output impedance in the presence of the filter is expressed as

$$Z_{\text{out}}^{\nu}(s) = Z_{\text{out}}^{\nu}(s)|_{Z_o=0} \cdot \frac{1 + Z_o(s)/Z_e^{\nu}(s)}{1 + Z_o(s)/Z_d^{\nu}(s)}. \tag{11}$$

The novel quantities $Z_d^{\nu}(s)$, $Z_n^{\nu}(s)$, $Z_g^{\nu}(s)$, and $Z_e^{\nu}(s)$ are found by measuring impedances at the port where the added circuit

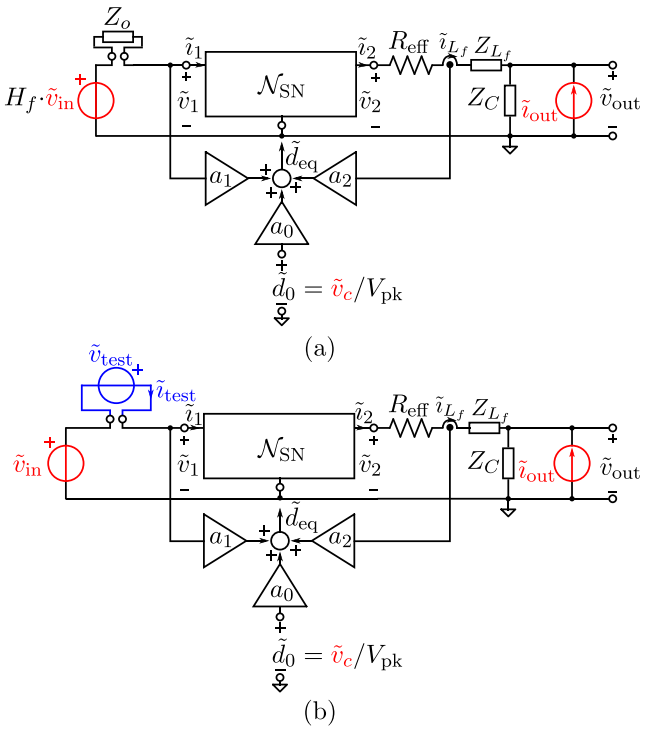

FIGURE 4 | High-level view of the averaged small-signal model shown in Figure 3. (a) The EMI filter is modeled as an extra element in the small-signal representation of Figure 3; (b) reference circuit model adopted for the computation of the impedances in (12)

TABLE 2 | Parameters of the main TFs of the small-signal circuit model in Figure 3.

	$V = \textbf{Trad}$	$V = \textbf{ZVS}$
k_{vc}^{ν}	e_0 / V_{pk}	$a_0 \cdot (e_0 / V_{\text{pk}})$
k_{vg}^{ν}	D_0	$D_{\text{eq}} + a_1 e_0$
$Z_1^{\nu}(s)$	$sL_f + R_{\text{eff}} + R_{L_f}$	$sL_f + R_{\text{eff}} + R_{L_f} - a_2 e_0$
$Z_2^{\nu}(s)$	$\left(\frac{1}{sC_{\text{out}}} + R_{C_{\text{out}}}\right) \| R_L$	$\left(\frac{1}{sC_{\text{out}}} + R_{C_{\text{out}}}\right) \| R_L$

element is introduced. Referring to Figure 4, these impedances are measured at the port where Z_o is connected to the rest of the small-signal model and are defined as

$$Z_d^{\nu}(s)=\left.\frac{\tilde{V}_{\text{test}}(s)}{\tilde{\imath}_{\text{test}}(s)}\right|_{\substack{\tilde{d}_0(s)=0\\ \tilde{v}_{\text{in}}(s)=0\\ \tilde{\imath}_{\text{out}}(s)=0}},\quad Z_n^{\nu}(s)=\left.\frac{\tilde{V}_{\text{test}}(s)}{\tilde{\imath}_{\text{test}}(s)}\right|_{\substack{\tilde{v}_{\text{in}}(s)=0\\ \tilde{\imath}_{\text{out}}(s)=0\\ \tilde{V}_{\text{out}}(s)\to 0}},$$
$$Z_e^{\nu}(s)=\left.\frac{\tilde{V}_{\text{test}}(s)}{\tilde{\imath}_{\text{test}}(s)}\right|_{\substack{\tilde{v}_{\text{in}}(s)=0\\ \tilde{d}_0(s)=0\\ \tilde{V}_{\text{out}}(s)\to 0}}\quad\text{and}\quad Z_g^{\nu}(s)=\left.\frac{\tilde{V}_{\text{test}}(s)}{\tilde{\imath}_{\text{test}}(s)}\right|_{\substack{\tilde{d}_0(s)=0\\ \tilde{\imath}_{\text{out}}(s)=0\\ \tilde{V}_{\text{out}}(s)\to 0}}, \tag{12}$$

where $\tilde{V}_{\text{test}}$ is applied at the Z_o port, while $\tilde{\imath}_{\text{test}}$ is the corresponding current response. The notation $\tilde{V}_{\text{out}}\to 0$ is adopted to indicate that the active input stimulus (i.e., the test voltage $\tilde{V}_{\text{test}}$ and the independent input perturbations $\tilde{d}_0$, $\tilde{\imath}_{\text{out}}$ and $\tilde{v}_{\text{in}}$ for Z_n^{ν}, Z_e^{ν} and Z_g^{ν}, respectively) are tuned so that $\tilde{V}_{\text{out}}$ is null. Based on (12) and the model in Figure 4 and through simple algebraic manipulations, the analytical expressions in Table 3 are derived. In the next section, design-oriented criteria are established based on the analytical expressions in Table 3.

3 | The EMI Filter Design Methodology

3.1 | The Design Criteria

The EET-based TFs derived in (9), (10), and (11) clearly highlight that the original behavior of the converter is not modified if the multiplying correction factors are, in magnitude, approximately equal to one. Accordingly, the inequalities

$$|Z_o(j\omega)|\ll|Z_n^{\nu}(j\omega)|,\quad |Z_o(j\omega)|\ll|Z_d^{\nu}(j\omega)|, \tag{13}$$

$$|Z_o(j\omega)|\ll|Z_e^{\nu}(j\omega)|,\quad |Z_o(j\omega)|\ll|Z_g^{\nu}(j\omega)|, \tag{14}$$

must be satisfied for any angular frequency ω. These conditions constitute conservative design criteria, as they ensure that the main converter TFs are not affected by the introduction of an EMI input filter. In consequence, they also permit to guarantee closed loop system stability if the control network is added a posteriori. Indeed, practical design criteria for the control network are typically established to achieve adequate stability margins and dynamic performances relying on the main TFs of the converter [1]. Since these TFs are not affected by the presence of the EMI filter, no degradation in performance or stability margins can occur.

In order to comply with these design criteria, $|Z_o(j\omega)|$ needs to be set with a margin m_{dB} typically ranging from 6 to 12 dB below the minimum of the EET impedance levels. According to the limits established by standard regulations for conducted emissions (e.g., CISPR/EN for Europe, FCC for North America) [22], the filter cutoff frequency f_c should be appropriately chosen to ensure compliance with the required attenuation $\text{A}tt_{\text{dB}}$ at the switching frequency, knowing that the LC filter exhibits a two pole roll-off at high frequencies:

$$10^{\frac{\text{Att}_{\text{dB}}}{20}}=\left(\frac{F_{\text{sw}}}{f_c}\right)^2. \tag{15}$$

From a practical filter design perspective, the chosen f_c leads to a scenario in which the minimum value of $|Z_d^{\nu}(j\omega)|$ constitutes the key design parameter, since under typical operating conditions, it represents the lowest impedance derived from the EET that $Z_o(s)$ must not exceed [1, 23].

Consequently, by focusing on $Z_d^{\nu}(s)$, the expression can also be written in the following form:

$$Z_d^{\nu}(s)=R_0^{\nu}\frac{\left(1+\frac{s}{\omega_0^{\nu}Q^{\nu}}+\frac{s^2}{(\omega_0^{\nu})^2}\right)}{\left(1+\frac{s}{\omega_1^{\nu}}\right)} \tag{16}$$

where the corresponding parameters are derived in Table 4 for both the traditional and QSW-ZVS modes.

TABLE 3 | Impedances derived with EET for traditional and QSW-ZVS operation modes.

	$\nu=\text{Trad}$	$\nu=\text{ZVS}$
$Z_d^{\nu}(s)$	$\frac{Z_1^{\text{Trad}}(s)+Z_2^{\text{Trad}}(s)}{D_0^2}$	$\frac{Z_1^{\text{ZVS}}(s)+Z_2^{\text{ZVS}}(s)}{D_0(D_{\text{eq}}+e_0a_1)}$
$Z_e^{\nu}(s)$	$\frac{Z_1^{\text{Trad}}(s)}{D_0^2}$	$\frac{Z_1^{\text{ZVS}}(s)}{D_0(D_{\text{eq}}+e_0a_1)}$
$Z_n^{\nu}(s)$	$-\frac{R_L}{D_0^2}$	$-\frac{e_0a_0}{I_{L_f}(D_{\text{eq}}+e_0a_1)}$
$Z_g^{\nu}(s)$	$\to+\infty$	$\to+\infty$

TABLE 4 | Parameters in the expression of Z_d^{ν} in traditional and QSW-ZVS operation modes.

	$\nu=\text{Trad}$	$\nu=\text{ZVS}$
R_0^{ν}	$\frac{R_L+R_{L_f}+R_{\text{eff}}}{D_0^2}$	$\frac{R_L+R_{L_f}+R_{\text{eff}}-e_0a_2}{D_0(D_{\text{eq}}+e_0a_1)}$
ω_0^{ν}	$\sqrt{\frac{R_{\text{eff}}+R_{L_f}+R_L}{L_fC_{\text{out}}(R_{C_{\text{out}}}+R_L)}}$	$\sqrt{\frac{R_{\text{eff}}+R_{L_f}+R_L-e_0a_2}{L_fC_{\text{out}}(R_{C_{\text{out}}}+R_L)}}$
Q^{ν}	$\frac{\sqrt{L_fC_{\text{out}}(R_L+R_{C_{\text{out}}})(R_{\text{eff}}+R_{L_f}+R_L)}}{L_f+C_{\text{out}}[R_L(R_{C_{\text{out}}}+R_{L_f}+R_{\text{eff}})+R_{C_{\text{out}}}(R_{L_f}+R_{\text{eff}})]}$	$\frac{\sqrt{L_fC_{\text{out}}(R_L+R_{C_{\text{out}}})(R_{\text{eff}}+R_{L_f}+R_L-e_0a_2)}}{L_f+C_{\text{out}}[R_L(R_{C_{\text{out}}}+R_{L_f}+R_{\text{eff}}-e_0a_2)+R_{C_{\text{out}}}(R_{L_f}+R_{\text{eff}})]}$
ω_1^{ν}	$\frac{1}{R_LC_{\text{out}}}$	$\frac{1}{R_LC_{\text{out}}}$

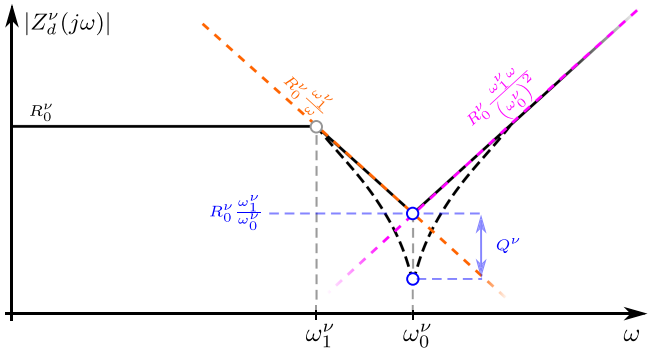

FIGURE 5 | Asymptotic construction of Bode plot of $|Z_d^\nu(j\omega)|$.

Studying the asymptotic behavior of $|Z_d^\nu(j\omega)|$ represented in the Bode plot of Figure 5, it can be noted that the DC value in the traditional and QSW-ZVS mode is expressed as R_0^ν. The response is then dominated by the first pole, which has an angular frequency equal to ω_1^ν, according to the corresponding case. By equating the two asymptotes, the intercept point occurs at $\omega = \omega_0^\nu$. With a first approximate analysis, the value at the intersection can be estimated by substituting ω_0^ν into the angular frequency variable in the expressions of the asymptotes, the resulting value being reported in Figure 5. Including the effect of the quality factor Q^ν, the value becomes equal to $R_0^\nu \omega_1^\nu / (Q^\nu \omega_0^\nu)$. A rigorous calculation, in turn, is carried out by substituting $\omega = \omega_0^\nu$ into the expression of $Z_d^\nu(s)$ in (16) and computing its magnitude, which provides the exact value of the minimum impedance relevant for the filter design:

$$\left|Z_d^\nu(j\omega_0^\nu)\right| = \frac{R_0^\nu}{Q^\nu}\sqrt{\frac{1}{1+(\omega_0^\nu/\omega_1^\nu)^2}}. \tag{17}$$

3.2 | The Optimized Design of the Damping Network

Considering the output impedance of an LC EMI filter, the reactive elements give rise to a resonance at a frequency equal to $f_f = \frac{1}{2\pi\sqrt{L_{\text{in}}C_{\text{in}}}}$. Consequently, to ensure that $Z_o(s)$ remains below the previously identified minimum value of $Z_d^\nu(s)$, adequate damping of the filter is required [24].

To determine the optimal values of the damping network components C_d and R_d, Middlebrook's approach is adopted [25], where the optimal damping condition is identified by minimizing the peaking of the output impedance $Z_o(s)$. To this end, the sensitivity of $Z_o(s)$ with respect to the filter quality factor is evaluated and set to zero, allowing the derivation of the critical frequency $f_{\text{opt}} = f_f\sqrt{\frac{2}{2+n}}$ at which the maximum peaking of $Z_o(s)$ occurs, with n denoting the ratio between the damping and the input capacitance. The output impedance is then evaluated at $\omega_{\text{opt}} = 2\pi f_{\text{opt}}$ and minimized, leading to the expressions of the optimal filter quality factor $Q_{f,opt}^\nu$ and the expression of n^ν in the considered operating modes [26, 27]:

$$n^\nu = \frac{R_{0f}\left(R_{0f} + \sqrt{R_{0f}^2 + 4(Z_{\text{target}}^\nu)^2}\right)}{(Z_{\text{target}}^\nu)^2}, \tag{18}$$

TABLE 5 | Buck converter component values.

Parameter	Value
Inductor L_{f}	8.2 µH
Inductor ESR $R_{L_{\text{f}}}$	7.5 mΩ
Output capacitor C_{out}	240 µF
Capacitor ESR $R_{C_{\text{out}}}$	1 mΩ
High-side switch $R_{\text{HS}_{\text{on}}}$	1 mΩ
Low-side switch $R_{\text{LS}_{\text{on}}}$	1 mΩ
Switching frequency F_{sw}	1 MHz
Output voltage V_{out}	5 V

TABLE 6 | Operating cases and corresponding parameter values.

	V_{in}	R_{L}	C_{SW}
Case I	20 V	0.33 Ω	4.1 nF
Case II	35 V	1.84 Ω	2.5 nF
Case III	45 V	3.35 Ω	3.19 nF

$$Q_{f,opt}^\nu = \sqrt{\frac{(4+3n^\nu)(2+n^\nu)}{2(n^\nu)^2(4+n^\nu)}}, \tag{19}$$

where $R_{0f} = \sqrt{L_{\text{in}}/C_{\text{in}}}$, while Z_{target}^ν corresponds to the target impedance that defines the upper limit for the maximum allowable value of the filter output impedance in traditional and QSW-ZVS cases, and it is defined as

$$Z_{\text{target}}^\nu = 10^{\frac{\left|Z_d^\nu(j\omega_0^\nu)\right|_{\text{dB}} - m_{\text{dB}}}{20}}. \tag{20}$$

The damping components for the two converter configurations are then calculated as $C_d^\nu = n^\nu \cdot C_{\text{in}}$ and $R_d^\nu = R_{0f} \cdot Q_{f,opt}^\nu$.

4 | Results Validation

To illustrate the application of the proposed methodology, a Buck converter characterized by the main parameter values listed in Table 5 is considered. Across its operating range, three illustrative cases, spanning the minimum, average, and maximum conditions of V_{in} and R_L (referred to as Case I, Case II, and Case III) are reported in Table 6, along with the corresponding C_{sw} values.

Based on filter design considerations outlined above and the optimal damping selection for the three considered cases, the EMI filter is implemented to satisfy the required EMI reduction for both the conventional converter and the QSW-ZVS operating mode. A target attenuation $Att_{\text{dB}} = 96\text{dB}$ is imposed, leading to the selection of a cutoff frequency approximately equal to $f_c \approx 3.8$ kHz, an inductance $L_{\text{in}} = 12$ µH, and a capacitance $C_{\text{in}} = 140$ µF. To ensure that the filter output impedance remains below the respective minimum of $Z_d^\nu(s)$ with a margin $m_{\text{dB}} = 10$ dB, the corresponding damping elements

are computed and reported in Table 7. The derived filters output impedance curves—$Z_o^{\text{Trad}}(s)$ for the traditional mode and $Z_o^{\text{ZVS}}(s)$ for QSW-ZVS operation—along with the evaluated $Z_d^v(s)$, are illustrated in Figure 6. The resulting relative reduction of the damping capacitance in QSW-ZVS mode, quantified for the three conditions in Table 7, demonstrates an overall improvement compared to the traditional case. Specifically, when the values of R_L and V_{in} are in the average and maximum conditions (i.e., Cases II and III), the requirement for a lower Z^v_{target}, related to a lower magnitude of the minimum of $Z_d^v(s)$, also depicted in Figure 6, becomes more stringent for the conventional operating mode. This necessitates a lower filter output impedance, which consequently results in a larger damping capacitance.

TABLE 7 | Damping network component values and size reduction comparison between capacitance in traditional and QSW-ZVS mode.

	C_d^{Trad}	R_d^{Trad}	C_d^{ZVS}	R_d^{ZVS}	C_d^{ZVS} % reduction
Case I	223.7 µF	310 mΩ	214.6 µF	320 mΩ	4.07%
Case II	276.7 µF	270 mΩ	27.6 µF	1.6 Ω	90.03%
Case III	231.4 µF	300 mΩ	2.6 µF	15.7 Ω	98.88%

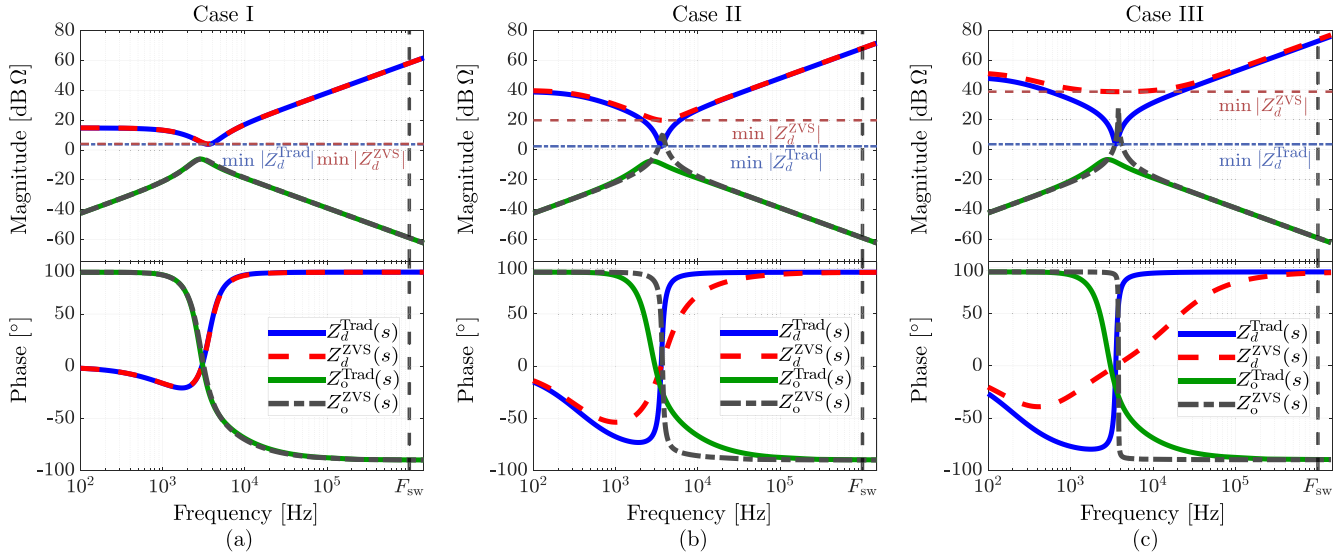

FIGURE 6 | Comparison of $Z_o^v(s)$ and $Z_d^v(s)$ with minimum impedance levels for damping network design for traditional and QSW-ZVS modes in Table 6. (a) Case I, (b) Case II, and (c) Case III.

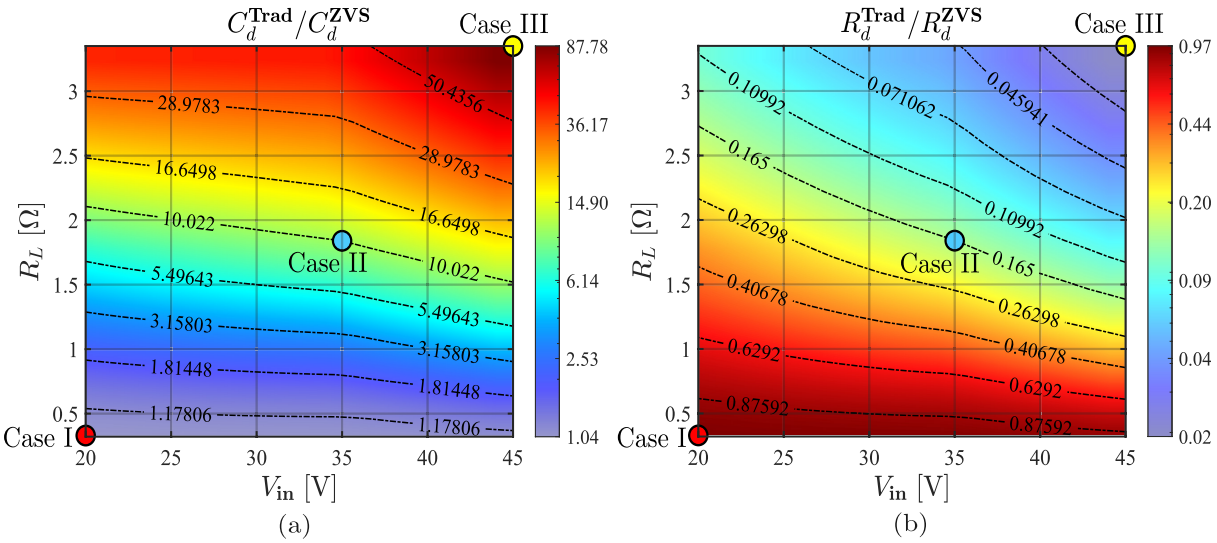

FIGURE 7 | Ratio of the values of the damping elements over the entire operating range of the Buck converter computed according to the criteria developed in Section 3. (a) Capacitance C_d^v and (b) resistances R_d^v. Cases I, II, and III in Table 6 are highlighted by red, blue, and yellow markers, respectively.

TABLE 8 | Selected components with physical dimensions of damping network capacitors.

Element	Value	Real component	Dim(mm)	Volume (mm^3)
Case I				
C_d^{Trad}	220 μ F	Wurth Elektronik 865060657012	Ø 10 × 10.5	824.7
C_d^{ZVS}	220 μ F	Wurth Elektronik 865060657012	Ø 10 × 10.5	824.7
Case II				
C_d^{Trad}	270 μ F	Panasonic EEE-FN1H271UP	Ø 10 × 10.2	801.1
C_d^{ZVS}	27 μ F	Wurth Elektronik 865080645009	Ø 6.3 × 7.7	240
Case III				
C_d^{Trad}	220 μ F	Wurth Elektronik 865060657012	Ø 10 × 10.5	824.7
C_d^{ZVS}	2.2 μ F	MURATA GCJ21BD71H225KE02L	2.0 × 1.25 × 1.25	3.13

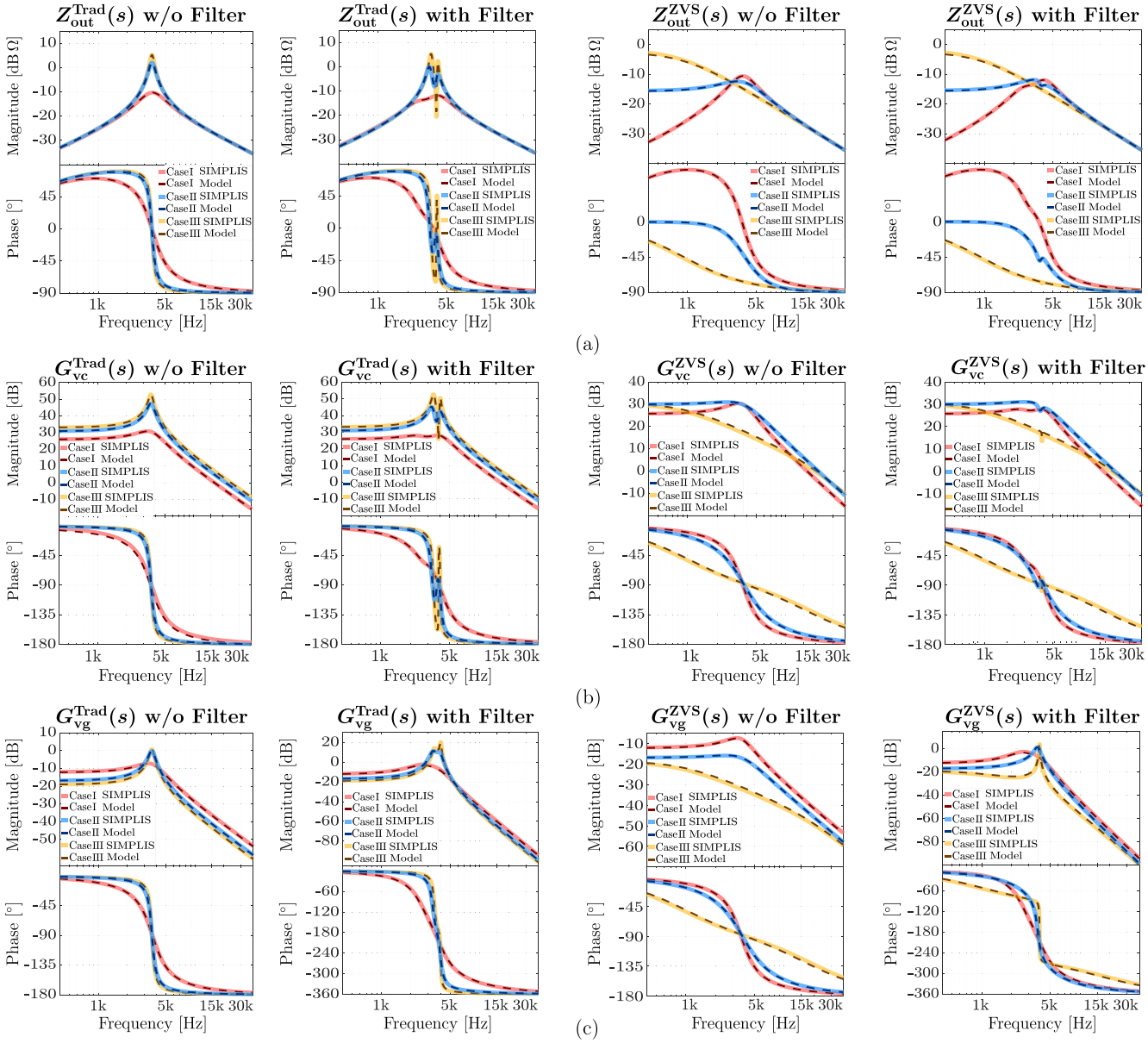

FIGURE 8 | TFs comparison without and with the EMI filter for both traditional and QSW-ZVS designs: (a) output impedance $Z_{\text{out}}^{\nu}(s)$, (b) control-to-output transfer function $G_{\text{vc}}^{\nu}(s)$, and (c) line-to-output transfer function $G_{\text{vg}}^{\nu}(s)$.

By extending this analysis over the entire range of R_L and V_{in} values, the results represented in Figure 7 are obtained. From the ratio of the corresponding damping capacitances and resistances for the traditional and QSW-ZVS mode, it can be observed that as R_L and V_{in} values increase, C_d^{Trad} becomes larger than C_d^{ZVS}, whereas the resistances follow the opposite trend, reaching the minimum difference between traditional and QSW-ZVS case at high values of R_L and V_{in}. However, considering practical implementation, the damping resistance has a negligible impact, since a larger damping capacitance dominates size and cost. This can be observed by selecting real components for the damping network, as reported in Table 8, which illustrates the variation in capacitance size between the conventional and QSW-ZVS cases. As for the damping resistances, they are specified with identical footprints, ensuring that their physical dimensions can be considered effectively equivalent in all cases. Therefore, within the considered conditions, the design without QSW-ZVS becomes more critical due to the increased capacitance values.

The same principles can be extended to cascaded filter sections or other filter topologies, provided that the resulting $Z_o(s)$ is appropriately considered. In all cases, the filter output impedance should remain below the minimum of the impedances derived with the EET. Notably, the difference between the minimum values of $Z_d^{Trad}(s)$ and $Z_d^{ZVS}(s)$ provides an additional design margin for the filter output impedance, enabling a more flexible selection of damping components in the QSW-ZVS configuration.

To validate the proposed small-signal model and the design methodology, the LC filter developed for the QSW-ZVS case is also applied to the conventional operating mode under the same three cases previously analyzed, allowing the assessment of its impact on the converter TFs. Extensive simulations are then carried out using SIMPLIS circuit simulator. The resulting TFs obtained from the analytical model and from simulations show strong agreement for both traditional and QSW-ZVS designs, as illustrated in Figure 8, thereby validating the accuracy of the small-signal model. The TFs $Z_{out}^{v}(s)$, $G_{vc}^{v}(s)$, and $G_{vg}^{v}(s)$ obtained both with and without the EMI filter further demonstrate that the filter designed for the QSW-ZVS case preserves the original converter behavior, in contrast, when QSW-ZVS is absent, the EET (13) and (14) are no longer satisfied, resulting in a modified system response.

To complete the study of C_d^{v} in the two operating modes, its frequency behavior is analyzed considering the case with intermediate values of R_L and V_{in} as a representative example (i.e., Case II). The filter cutoff frequency is swept over a range of frequencies, thereby covering the filter design cases corresponding to different Att_{dB} requirements, and the relative variation of the damping capacitance in QSW-ZVS condition with respect to the conventional case is evaluated, as depicted in Figure 9. A tracking line $Z_{track}^{Trad}(s)$ for conventional converter and $Z_{track}^{ZVS}(s)$ for QSW-ZVS mode, representing the minimum value among $Z_n^{v}(s)$, $Z_d^{v}(s)$, and $Z_e^{v}(s)$, is reported in the plot as a dashed blue line for the conventional case and as a solid red for the QSW-ZVS one. Depending on the frequency interval in which f_c lies, the behavior is dominated by a different impedance derived with the EET. Specifically,

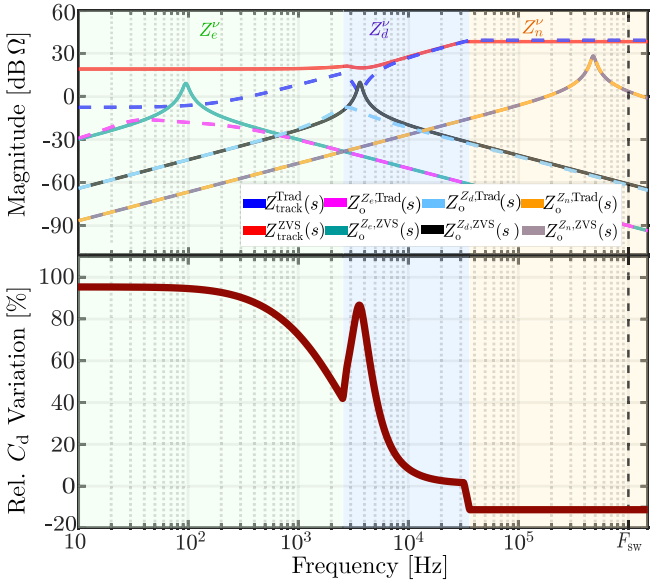

FIGURE 9 | EMI filter output impedances with different f_c designed to be constrained below the respective tracking lines, for traditional and QSW-ZVS mode. The bottom panel illustrates the relative variation of C_d^{ZVS} with respect to traditional case across the frequency.

in the first region, with a green background, the $Z_e^{v}(s)$ term is predominant, in the second one highlighted in blue, $Z_d^{v}(s)$ becomes critical for the filter design, and in the last orange section, the behavior is governed by $Z_n^{v}(s)$. In each of these areas, an illustrative example of the filter output impedance is identified as $Z_o^{Z_e v}(s)$, $Z_o^{Z_d v}(s)$, and $Z_o^{Z_n v}(s)$ depending on the dominant impedance along the tracking line to which it is constrained, either under the QSW-ZVS or conventional condition. By computing the relative percentage variation of C_d^{ZVS} compared to traditional case, the curve in the lower portion of the plot is obtained. The maximum reduction of C_d^{ZVS} with respect to the conventional case occurs when the filter is centered at low frequencies, where the tracking line is dominated by $Z_e^{v}(s)$, and when it falls below the minimum of $Z_d^{v}(s)$. As the frequency increases and the $Z_n^{v}(s)$ curve becomes predominant, the overall trend slightly changes, since $Z_n^{ZVS}(s)$ exhibits a lower magnitude compared to the traditional case. Focusing on the central frequency region, which represents the practical range of interest for typical attenuation requirements, the QSW-ZVS technique is consistently advantageous for the design of a smaller and more compact EMI filter, as it requires a lower value of damping capacitor.

5 | Conclusions

This paper presents a comprehensive small-signal analysis of the QSW-ZVS buck converter and its interaction with an input passive LC EMI filter. A complete small-signal model is derived to capture the resonant effects introduced by QSW-ZVS operation.

Through application of the EET, the effects of the EMI filter on converter TFs are systematically analyzed. The design methodology ensures that the passive EMI filter does not influence the converter behavior, thereby preserving its dynamic

performance is presented. The approach determines appropriate damping network components' values across different operating points. Simulation results obtained in SIMPLIS validate the accuracy of the analytical model and the effectiveness of the design procedure.

A comparison of the required damping capacitance under different operating conditions and as a function of frequency is performed for the QSW-ZVS and conventional cases, demonstrating that, when QSW-ZVS technique is applied, the design of practical damping network leads to a more compact EMI filter through a reduction in the damping capacitance value.

Acknowledgments

This publication is part of the project PNRR-NGEU, which has received funding from the MUR-DM 352/2022. Open access publishing facilitated by Politecnico di Torino, as part of the Wiley - CRUI-CARE agreement.

The authors would like to thank Davide Lena and the entire STMicroelectronics team in Turin for the support.

Conflicts of Interest

The authors declare no conflicts of interest.

Data Availability Statement

The data that support the findings of this study are available from the corresponding author upon reasonable request.

References

1. R. W. Erickson and D. Maksimovic, *Fundamentals of Power Electronics* (Springer Science & Business Media, 2007).

2. M. K. Kazimierczuk, *Pulse-Width Modulated DC-DC Power Converters* (John Wiley & Sons, 2015).

3. A. S. Emara, D. Romanov, G. W. Roberts, S. Aouini, M. Parvizi, and N. BenHamida, "Optimized Periodic ΣΔ Bitstreams for DC Signal Generation Used in Dynamic Calibration Applications," *IEEE Open Journal of Circuits and Systems (O-CAS)* 1, no. 1 (2020): 3–12.

4. B. Majmunović, B. A. McDonald, S. Y. Yu, and J. Strydom, "90°-Valley Unified Controller for Zero-Voltage-Switching Quasi-Square-Wave (ZVS-QSW) Boost Converter," *IEEE Transactions on Power Electronics* 39, no. 6 (2024): 6930–6940.

5. F. Karakaya, Ö. Gülsuna, and O. Keysan, "Feasibility of Quasi-Square-Wave Zero-Voltage-Switching Bi-Directional DC/DC Converters With GaN HEMTs," *Energies* 14, no. 10 (2021): 2867.

6. S. Sharifi, M. Jabbari, and H. Farzanehfard, "A New Family of Single-Switch ZVS Resonant Converters," *IEEE Transactions on Industrial Electronics* 64, no. 6 (2017): 4539–4548.

7. H. Bodur and A. F. Bakan, "A New ZVT-ZCT-PWM DC-DC Converter," *IEEE Transactions on Power Electronics* 19, no. 3 (2004): 676–684.

8. Z. Zhang and K. D. T. Ngo, "Multi-Megahertz Quasi-Square-Wave Flyback Converter Using eGaN FETs," *IET Power Electronics* 10, no. 10 (2017): 1138–1146.

9. I. Stevanovic and B. Wunsch, *Electromagnetic Modeling in Power Electronics* (MDPI-Multidisciplinary Digital Publishing Institute, 2021).

10. Y. Saito, T. Ibuchi, T. Funaki, K. Kawai, and T. Tsuda, "A Study on EMI Noise Source Modeling With Voltage Source in Synchronous DC-DC Buck Converter," in *2020 IEEE 11th International Symposium on Power Electronics for Distributed Generation Systems (PEDG)* (IEEE, 2020), 470–475.

11. B. Narayanasamy and F. Luo, "A Survey of Active EMI Filters for Conducted EMI Noise Reduction in Power Electronic Converters," *IEEE Transactions on Electromagnetic Compatibility* 61, no. 6 (2019): 2040–2049.

12. B. Choi, D. Kim, D. Lee, S. Choi, and J. Sun, "Analysis of Input Filter Interactions in Switching Power Converters," *IEEE Transactions on Power Electronics* 22, no. 2 (2007): 452–460.

13. R. D. Middlebrook and S. Cuk, "A General Unified Approach to Modelling Switching-Converter Power Stages," in *1976 IEEE Power Electronics Specialists Conference* (IEEE, 1976), 18–34.

14. J. Chen, Y. Han, Q. Han, and Q. Liu, "A DPWM-Based Quasi-Constant Switching Frequency Control for Full ZVS Range Three-Phase Inverter With Reactive Power Transfer Capability," *IEEE Transactions on Industrial Electronics* 70, no. 5 (2022): 4912–4921.

15. M. Jabbari and M. Mokhtari, "High-Frequency Resonant ZVS Boost Converter With Grounded Switches and Continuous Input Current," *IEEE Transactions on Industrial Electronics* 67, no. 2 (2019): 1059–1067.

16. F. Gabriele, F. Pareschi, G. Setti, R. Rovatti, D. Lena, and M. R. Borghi, "Small-Signal Circuit Model for Synchronous Buck DC/DC Converter Featuring ZVS at Low-Side," in *2023 IEEE International Symposium on Circuits and Systems (ISCAS)* (IEEE, 2023), 1–5.

17. G. Liu, H. Ouyang, and M. Xiao, "Optimal Design of High Frequency High Efficiency and High-Power Density DC–DC Power Module Based on GaN," *IET Power Electronics* 16, no. 10 (2023): 1667–1682.

18. F. Gabriele, F. Pareschi, G. Setti, et al., "Small-Signal Model of a Boost Converter Exploiting ZVS at the High-Side MOSFET," in *2024 IEEE 67th International Midwest Symposium on Circuits and Systems (MWSCAS)* (IEEE, 2024), 1352–1356.

19. M. K. Kazimierczuk, *Pulse-Width Modulated DC-DC Power Converters*, 2nd ed. (Wiley, 2015).

20. V. Vorperian, "Simplified Analysis of PWM Converters Using Model of PWM Switch. Continuous Conduction Mode," *IEEE Transactions on Aerospace and Electronic Systems* 26, no. 3 (1990): 490–496.

21. V. Vorperian, *Fast Analytical Techniques for Electrical and Electronic Circuits* (Cambridge University Press, 2002).

22. T. Hegarty, "An Overview of Conducted EMI Specifications for Power Supplies," in *SLYY136* (Texas Instruments Incorporated: 2018).

23. H. Zhang, "Simple Solution for Input Filter Stability Issue in DC/DC Converters" *SLUA929A*, Texas Instruments Application Report, 2019.

24. D. M. Mitchell, "Power Line Filter Design Considerations for DC-DC Converters," *IEEE Industry Applications Magazine* 5, no. 6 (1999): 16–26.

25. R. D. Middlebrook, "Input Filter Considerations in Design and Application of Switching Regulators," *IEEE Industry Applications Society Annual Meeting* (1976) Record: 366–382.

26. R. W. Erickson, *Optimal Single Resistors Damping of Input Filters* (IEEE APEC Annual Applied Power Electronics Conference and Exposition, 1999).

27. L. Xing, F. Feng, and J. Sun, "Optimal Damping of EMI Filter Input Impedance," *IEEE Transactions on Industry Applications* 47, no. 3 (2011): 1432–1440.